Available online at www.sciencedirect.com
SCIENCE DIRECT®
International Journal of Heat and Mass Transfer 49 (2006) 2782–2792
International Journal of HEAT and MASS TRANSFER
www.elsevier.com/locate/ijhmt

High heat-flux accelerator targets: Cooling with liquid metal jet impingement

I. Silverman [a], A.L. Yarin [b,c,*], S.N. Reznik [b], A. Arenshtam [a], D. Kijet [a], A. Nagler [a]

[a] *Soreq NRC, Yavne 81800, Israel*
[b] *Faculty of Mechanical Engineering, Technion – Israel Institute of Technology, Haifa 32000, Israel*
[c] *Department of Mechanical and Industrial Engineering, University of Illinois at Chicago, 842 West Taylor Street, Chicago, IL 60607-7022, United States*

Received 30 August 2005; received in revised form 20 February 2006
Available online 18 April 2006

Abstract

In order to evaluate the performance of jet impingement for high heat-flux cooling, experimental cooling loops based on water and liquid metal jet impingement were designed and constructed. The current liquid metal system, based on an eutectic alloy of gallium and indium (GaIn) with a melting point of 15.7 °C, employs an annular inductive electromagnetic pump. The experiments showed that it is capable of accommodating a heat flux of about 20 MW/m^2 over an area of 10^{-4} m^2. The jet velocity is less than 4 m/s and the required differential pressure from the pump is less than 10^5 Pa.

In the present work the experimental section is supplemented by a theoretical one in which the cooling capability of impinging jets of liquid metal is modeled. In particular, turbulent flow in a dead end associated with the rear surface of a high-temperature target, and the corresponding heat-transfer process, are considered. The developed novel analytical model embodies the main peculiarities of the heat-transfer process and agrees fairly well with the experimental data. In addition, a detailed direct numerical simulation was done with the STAR-CD code. The gross underprediction of the turbulent heat transfer rate by the STAR-CD code is attributed to overprediction of the eddy viscosity in liquid metal flows.

1. Introduction

In accelerator systems, the interaction of the particle beam with the target generates a very high density of thermal energy. The total power for radioisotope production targets is of the order of 10–50 kW. Typically, the geometric size of the target is very small and the heat flux very high. Normal average heat fluxes from these targets are around 10 MW/m^2 and may reach levels of an order of magnitude higher at hot spots. Efficient heat removal techniques are needed to preserve the integrity of the target, especially where such high heat fluxes are involved. One technique based on jet-impingement has been shown to be able to deal with fluxes up to 400 MW/m^2, over an area of a few square millimeters, with water as coolant [1]. Blackburn et al. used this technique to develop a high-power target for production of neutrons in an accelerator [2]. Lienhard [3] provides a detailed review of the research work done on this technique. Recently, Mitsutake and Monde [4] and Zhen-Hua et al. [5] also studied the heat fluxes removable by water jets.

With water as coolant, very high jet velocities – more than 100 m/s – are needed for heat fluxes of 400 MW/m^2. A possible improvement might be achieved by using a liquid metal (such as gallium or gallium-based alloy), which significantly improves the heat transfer efficiency of the jet [3,6]. Blackburn and Yanch [7,8] used this technique to improve the performance of their accelerator target for

* Corresponding author. Address: Department of Mechanical and Industrial Engineering, University of Illinois at Chicago, 842 West Taylor Street, Chicago, IL 60607-7022, United States. Tel.: +1 312 996 3472; fax: +1 312 413 0447.
E-mail address: ayarin@uic.edu (A.L. Yarin).

0017-9310/$ - see front matter © 2006 Elsevier Ltd. All rights reserved.
doi:10.1016/j.ijheatmasstransfer.2006.02.038

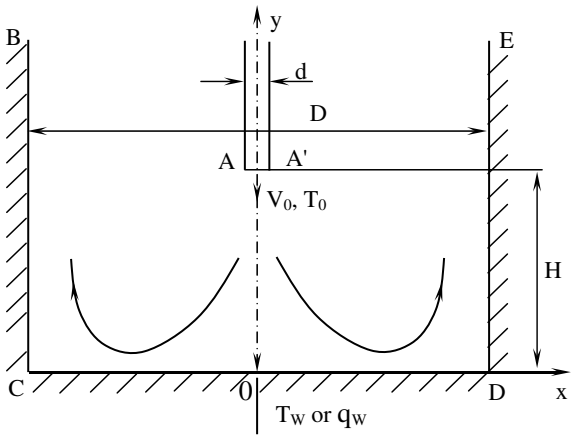

Fig. 1. Jet issued from the nozzle AA′ into a submerged dead-end BCODE.

BNCT (Boron Neutron Capture Therapy). Recently, Miner and Ghoshal [9] presented results for a miniature gallium jet impingement system for cooling high-power microelectronic devices.

Numerous works in literature deal with axisymmetric and planar jets of air and water impacting onto targets. Most of them are experimental, but in a number of publications semi-empirical turbulence models were used for semi-analytical or direct numerical simulation. The flow structure is shown in Fig. 1. It should be noted that in many cases the outer confinement BC, DE was absent, and in this sense the impinging jets were free. The dependences for the Nusselt number Nu at the stagnation point of the axisymmetric air and water jets follow the scaling law $Nu \sim Re^{0.5}Pr^{0.33}$ for $1 \leqslant H/d \leqslant 10$ (Re being the Reynolds number, H the distance to the target and d the nozzle diameter). For planar jets the scaling is $Nu \sim Re^{0.6}Pr^{0.33}$ for $1 \leqslant H/d \leqslant 8$. Additional empirical correlations for the heat-transfer coefficient in impinging water jets can be found in [4].

In contrast to the above, works on jets of liquid metals are rather scarce. Lienhard [3] argued that due to the low Prandtl numbers of liquid metals, the correlations for laminar flows also hold for turbulent conditions. The correlation by Sato et al. [6] was proposed for the case where hot liquid metal jet impinges on a cold plate and partially melts its surface. Both these correlations demonstrate the high potential of gallium as a substitute for water.

The aim of the present work is experimental and theoretical investigation of the heat transfer in impinging jets of a GaIn alloy versus water. Section 2 describes the experimental setup and the alloy used. The experimental results are summarized in Section 3. Section 4 presents an analytical model of the heat transfer near the stagnation point of an impinging liquid metal jet, and compares its predictions with the experimental data. Section 5 describes the direct numerical simulation with the corresponding comparison. Conclusions are drawn in Section 6.

2. Experimental setup

In order to evaluate the actual potential of jet impingement for high heat flux cooling, experimental cooling loops were designed. Fig. 2 presents a schematic of such a loop with an electron-gun heat source, and Tables 1 and 2 present the parameters used for liquid metal and water cooling.

The initial results with the water impingement system yielded a cooling capacity of 5 kW with an average heat flux of 5 MW/m^2 and a maximum of about 10 MW/m^2 with a total target area of 10^{-3} m^2 [10].

For the liquid metal system, there is a choice of available coolants, including metals and alloys that are liquid at

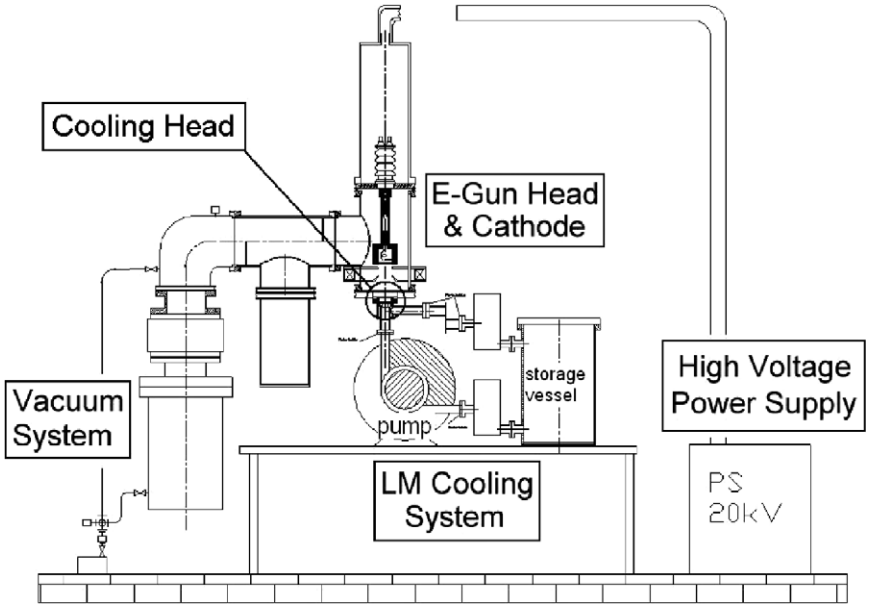

Fig. 2. Schematic diagram of the liquid metal cooling loop and an electron heat source.

Table 1
Nominal, minimal and maximal design values for liquid metal experimental cooling loop

Parameter	Minimum value	Nominal value	Maximum value
Power [kW]	0	15	20
Heat flux [MW/m^2]	0	10	50
Flow rate [l/s]	0	0.5	0.5
Jet velocity [m/s]	0	10	10
Jet diameter [mm]	5	5	12
Jet distance [mm]	4	4	20
Coolant temperature [°C]	40	50	75
Wall temperature [°C]	40	200	200
Coolant pressure [10^5 Pa]	1	1	1.5
Inlet pressure [10^5 Pa]	1	9	9.5

Table 2
Nominal, minimal and maximal values for water experimental cooling loop

Parameter	Minimum value	Nominal value	Maximum value
Power [kW]	0	15	20
Heat flux [MW/m^2]	0	10	50
Flow rate [l/s]	0	2.5	3
Jet velocity [m/s]	0	50	60
Jet diameter [mm]	5	8	12
Jet distance [mm]	4	4	20
Coolant temperature [°C]	20	30	50
Wall temperature [°C]	20	200	200
Coolant pressure [10^5 Pa]	1	5	5
Inlet pressure [10^5 Pa]	1	25	32

room temperature. Table 3 presents reference properties of some of the latter. Mercury has toxicology problems and NaK is reactive and entails special safety considerations. Hence, we preferred to work with a gallium alloy (the melting point of gallium is too high to ensure that it is liquid without a special heating system), namely a GaIn eutectic that can be kept liquid with normal room heating even on cold winter days in Israel.

The cooling system shown in Fig. 2 comprises three components: (1) the cooling head, (2) an electro-magnetic pump, and (3) a storage tank with a built-in heat exchanger. In particular, a four liter storage vessel incorporates a water-cooled heat exchanger. The GaIn alloy is placed in the vessel and a protective Argon gas fills the rest of the vessel and provides static pressure which can be adjusted. The heat exchanger is placed in the vessel to cool the GaIn alloy. A pipe from the bottom of the vessel supplies GaIn alloy to the pump. The electro-magnetic pump, of the annular induction type, was assembled in situ by removing the rotor of a standard 2 kW electric motor and mounting the pump body inside the original stator, with the attendant change in the system impedance and hence in the current in the stator coils. The efficiency of the pump being much lower than that of the motor, the heat generated in it is higher than calculated for the former and the original cooling fins and fans are not enough to keep it cold. Thus it has to be kept in a bath of cooling oil in order to prevent its monitored temperature from exceeding the operating limit. The electric power to the pump is supplied through a three-phase variac, whose outlet voltage controls the flow rate of the liquid metal in the loop. The pump is a part of a required vacuum-tight system which protects the GaIn alloy from oxidation.

Fig. 3a shows the cooling head for the liquid metal system, and Fig. 3b – details of the target disk and the thermocouple locations. The target disk is made of TZM alloy (Mo 99.4%, Ti 0.5%, Zr 0.08%, C 0.02% by weight), so as to ensure both high thermal conductivity and high strength up to high temperatures. Its thickness is 2 mm. The nozzle placed about $H = 4$ mm from the target, is a $d = 5$ mm hole in a cup at the top of a 16 mm ID straight tube. Its shape ensures an almost uniform velocity profile of the outgoing flow. The target temperature is measured at four different locations by K-type thermocouples. The thermocouples are places at the end of radially drilled holes (see Fig. 3b). The axes of these drills are 1 mm bellow the heated surface. The thermocouples are mineral isolated and have diameter of 0.5 mm. All the thermocouples are at the same distance from the heated surface but at different radial positions from its center. The other measurement sensors installed in the system are two thermocouples connected to the liquid-metal pipes at the inlet and outlet of the cooling head. Their readings are used to calculate the

Table 3
Physical parameters of several coolants

Parameter	Water	Gallium	GaIn	NaK	Hg
Composition			77% Ga, 23% In	78% K, 22% Na	
Melting temperature [°C]	0.0	29.8	15.7	−11.1	−38.8
Boiling temperature [°C]	100.0	2205	2000	783.8	356.8
Density [kg/m^3]	1000	6100	6280	872	13599
Heat capacity [J/kg K]	4181	373	326	1154	140
Thermal conductivity [W/m K]	0.61	28	41.8	25.3	7.8
Viscosity [10^{-3} kg/m s]	0.855	1.96	1.69	0.468	1.55
Kinematic viscosity [10^{-8} m^2/s]	85.5	32	27	53.7	11.4
Prandtl number [–]	5.86	0.0261	0.0204	0.0213	0.0278

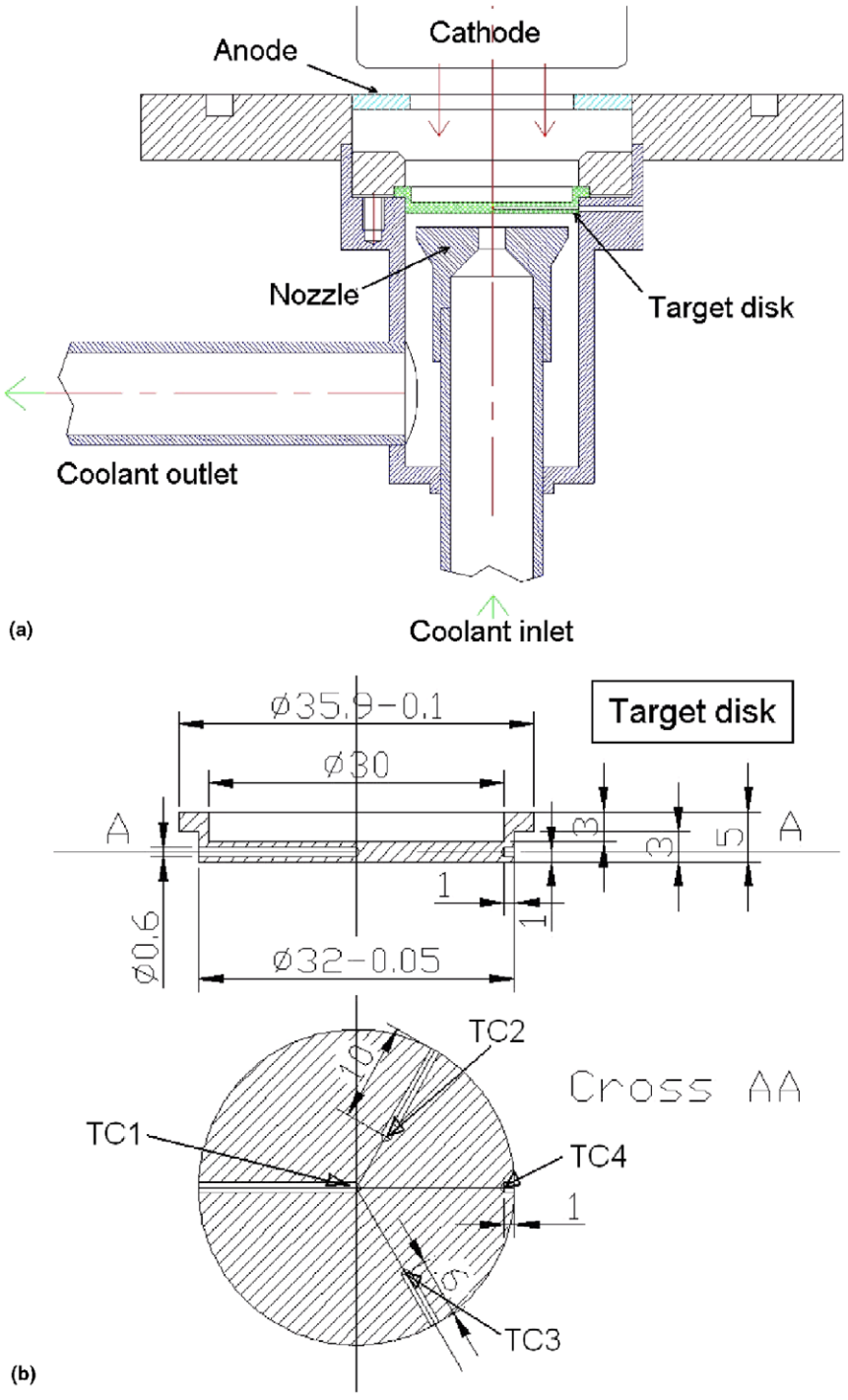

Fig. 3. (a) A cut through the cooling head and (b) details of the target and thermocouple locations.

temperature increase in the coolant as it passes through the cooling head.

To prevent oxidation of the liquid metal, the system is vacuum-tight. The pipes of all components are connected together with CF flanges with nickel gaskets. The flange at the top of the cooling head is used to connect it to the electron-gun heating source (with a 1 Hz on/off controller), of which the cathode in Fig. 3a forms a part.

3. Experimental results

The results presented in Fig. 4 are from an experiment for which the electron gun was set to heat a circular area 10 mm in diameter, with its power increased in steps up to 9 MW/m^2. The voltage to the pump was changed a few times to regulate the flow rate.

Fig. 4 presents the beam power density and the resulting target and coolant temperatures. The thermocouple

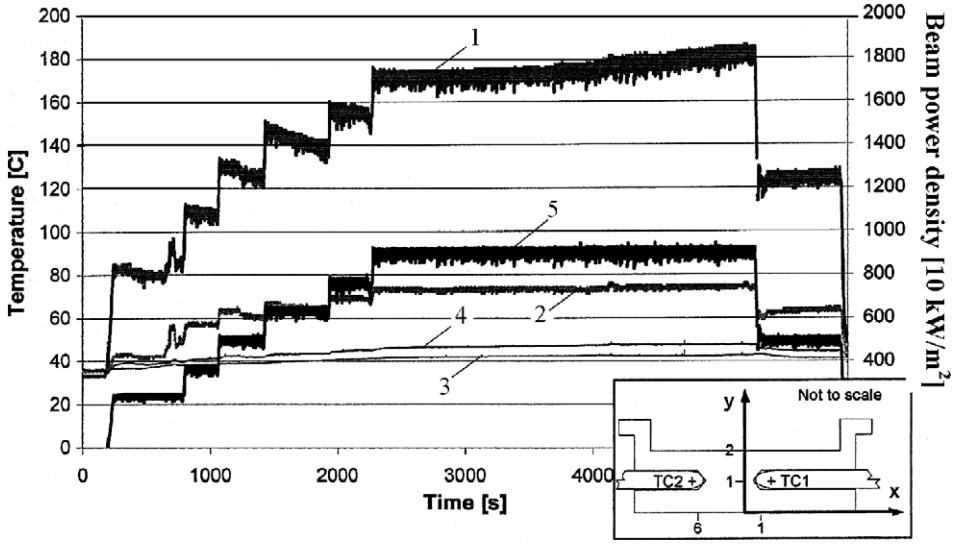

Fig. 4. Results of the medium power experiment with 10 mm diameter heating area. The insert shows the radial and axial locations of the thermocouples and the coordinate system. (1) Temperature measured by the first thermocouple TC1, (2) by the second thermocouple TC2, (3) coolant temperature at the entrance, (4) coolant temperature at the exit, (5) beam power. GaIn alloy as the working liquid.

inserted to a distance of $x = 1$ mm from the center is marked TC1, and the other thermocouple, inserted to a distance of $x = 6$ mm is marked TC2 (cf. the insert in Figs. 4 and 3b). As can be seen, the target temperature responds immediately to any change in the beam power. The target's heating rate is thousands of degrees per second, due to its very low thermal mass relative to the beam power density (2000 K/s for a power of 10 MW/m^2). The fluctuations are due to the electron-gun heat source. The heating power is a function of the cathode temperature which determines the electrons current. The cathode is heated by a filament and loses heat by radiation. The heating power is controlled by measuring the beam current and turning on or off the filament heating. The measurement rate of the current control system (1 Hz) causes time delays which generate the fluctuations seen in Figs. 4 and 5.

The low differential pressure generated by the pump and materials compatibility prevented us from using standard commercial flow meters. We tried to install an electro-magnetic flow meter but did not get any signal. Hence, the flow rate was not measured directly but calculated from the gun power and the temperature difference between the outlet and inlet to the cooling head as follows. The cooling and heating rates of the target are $Q_{\text{cooling}} = Fc_p\ (T_{\text{out}} - T_{\text{in}})$ and $Q_{\text{heating}} = IV$, respectively, where F is the coolant mass flow rate, T_{out} and T_{in} are the coolant temperatures at the outlet and inlet of the cooling head, c_p is the specific heat at constant pressure. Losses to the environment are

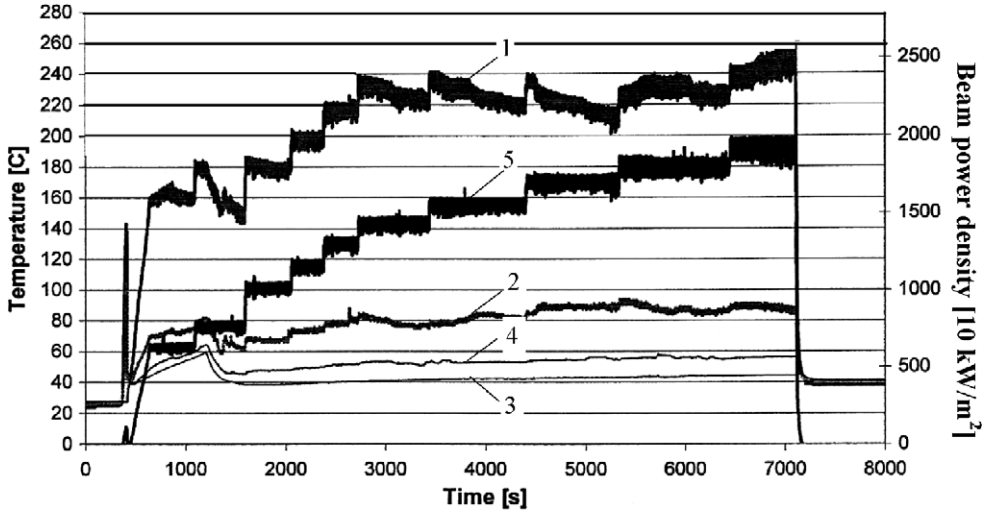

Fig. 5. Results of the high power experiment with 10 mm diameter heating area. (1) Temperature measured by the first thermocouple, (2) by the second thermocouple, (3) coolant temperature at the entrance, (4) coolant temperature at the exit, (5) beam power. GaIn alloy as the working liquid.

less than 10%. Therefore, $Q_{\text{cooling}} \simeq Q_{\text{heating}}$ and $F = IV/[c_p(T_{\text{out}} - T_{\text{in}})]$, which was used to calculate F for the GaIn cooling system in the present work (note that in [10] F was measured directly for water-cooling system).

The calculated GaIn jet velocities during the experiment were 2–6 m/s. The Reynolds number based on the nozzle diameter was 40,000–110,000, which implies a turbulent flow.

In the next experiment the beam power density was increased up to about 20 MW/m^2. The results are presented in Fig. 5. This experiment was discontinued at a beam power level of about 1.6 kW because of surface heating of the cooling head, which caused melting of the solder seals in the thermocouple holes and leakage of the alloy.

Thermocouple TC1 measured a temperature of about $T_{\ell 1} = 230 \pm 5$ °C at cooling jet velocity $V_0 = 2.35 \pm 0.1$ m/s and heating power $q_{\text{w}} = 14 \pm 0.5$ MW/m^2. Under the same conditions TC2 measured $T_{\ell 2} \simeq 80$ °C. For cooling jet velocity $V_0 = 3.25 \pm 0.2$ m/s and heating power $q_{\text{w}} = 19 \pm 1$ MW/m^2, TC1 measured $T_{\ell 1} \simeq 248 \pm 10$ °C, TC2 $- T_{\ell 2} \simeq 85$ °C.

3.1. Measurement accuracy analysis

For a complete picture of the experimental results, an error analysis is needed to understand the inaccuracies associated with them. We first consider limitations due to the nature of the system. The thermocouples with a diameter of 0.5 mm are of the mineral insulated type with a stainless steel sleeve. For heat fluxes in the range of 10–20 MW/m^2 and thermal conductivity of 126 W/(m K) for TZM, the temperature gradient in the target is about 8×10^4–16×10^4 K/m. This alone entails an uncertainty of ±20 to 40 K in the target temperature. In addition there are the mechanical tolerances in the drilling of the hole that add an uncertainty of about ±0.1 mm in the actual location of the center of the thermocouple. The inaccuracies of the thermocouples themselves and of the A/D converters are negligible in comparison.

A second source of uncertainty is the behavior of the heat source. Heating power of the electron gun being controlled by a 1 Hz on/off controller, the beam power fluctuates about ±5%, and the target temperature – a few degrees. The error bars are given above with the data.

A third source of uncertainty is a slight drift in the target temperature, in spite of the fact that the average beam power was kept constant at each step. This might be due to changes in interface conditions or in the flow rate, which was not measured directly while some changes were made in the power to the pump. (All flow velocities given here were calculated from the heat power and the temperature differences between the outlet and inlet, as was mentioned above). For these reasons we did not try to calculate the actual heat transfer coefficient corresponding to the measurements, and made do with measuring the target temperature. Thus the results provided by the current system are mostly qualitative. In order to get quantitative results the system should be improved, the spatial power profile of heat source measured, and the wall temperature determined with higher spatial resolution.

4. Analytical model of heat transfer near the stagnation point in liquid metal jets

4.1. Problem formulation

Consider a jet of a liquid metal issued into a dead end (Fig. 1). The nozzle is coaxial with the dead-end BCODE. In the axisymmetric case the nozzle and the dead end are cylinders of diameters d and D, respectively; in the planar case they are slits of thicknesses d and D, respectively. The planar case is also representative of a dense system of jets aligned along the line normal to the plane x, y in the figure. The distance from the nozzle exit to the bottom of the dead end is denoted by H. The velocity and temperature of the jet at the nozzle exit are denoted V_0 and T_0, respectively, while the temperature of the bottom of the dead end is T_{w} (a fixed temperature; the boundary condition with fixed thermal flux will also be discussed). The walls BC and DE can be considered as thermally insulated. The aim of the present section is to calculate the heat transfer rate at the bottom of the dead end CD. In particular, the case of jet cooling will be discussed, where $T_{\text{w}} > T_0$.

4.2. Physical estimates

The heat flux in turbulent flows, $\mathbf{q}$, depends on both molecular and eddy transfer mechanisms [11]

$$\mathbf{q} = -\rho c_p \left(\frac{\nu}{Pr} + \frac{\nu_{\text{T}}}{Pr_{\text{T}}} \right) \nabla T. \tag{1}$$

Here ρ is the density, c_p is the specific heat at constant pressure, ν and Pr are the kinematic viscosity and molecular Prandtl number, while ν_{T} and Pr_{T} are their turbulent (eddy) counterparts, respectively; ∇T is the gradient of the averaged temperature. The molecular and turbulent thermal diffusivities, κ and κ_{T}, are given by

$$\kappa = \frac{\nu}{Pr}, \quad \kappa_{\text{T}} = \frac{\nu_{\text{T}}}{Pr_{\text{T}}}. \tag{2a, b}$$

Pr_{T} is known to be always close to 1, since both momentum and heat are transferred by the same eddies. On the other hand, Pr can significantly differ from 1, since molecular transfer of momentum and heat can have a different physical background. This is, in particular, the case with liquid metals, where, for example, for GaIn alloy $Pr = 0.0204$ (Table 3).

Turbulent viscosity is typically much higher than its molecular counterpart. Therefore, in the case of fluids with $Pr = \text{O}(1)$, Eqs. (2a,b) yield $\kappa_{\text{T}} >> \kappa$, and the molecular thermal diffusivity can be neglected. In this case $\mathbf{q} = -\rho c_p(\nu_{\text{T}}/Pr_{\text{T}})\nabla T = -\rho c_p \kappa_{\text{T}} \nabla T$. However, for liquid metals, where $Pr << 1$ the molecular mechanism of heat transfer may overbear the turbulent one depending on the values

of v and v_T. For GaIn alloy $v = 27 \times 10^{-8}$ m^2/s (Table 3). To estimate v_T, we assume that the turbulence intensity in the jet with axis AO in Fig. 1 is less than that of the mixing layers at its edges. An appropriate expression for v_T in the latter is given by Prandtl's formula [11], which in the present case takes the form

$$v_T = KV_0(H - y), \tag{3a}$$

$$v_{T,max} = KV_0H. \tag{3b}$$

The value of the empirical coefficient is $K = 0.0055/4 = 0.001375$ [12,13]. Taking for the estimate $V_0 = 1$ m/s and $H = 0.4 \times 10^{-2}$ m, we find $v_{T,max} = 0.55 \times 10^{-5}$ m^2/s. Therefore, for $Pr_T = 1$ according to Eq. (2b) $\kappa_{T,max} = 0.55 \times 10^{-5}$ m^2/s. On the other hand, for GaIn $\kappa = v/Pr = 1.324 \times 10^{-5}$ m^2/s (Table 3). Since this value is about three times that of κ_T, we can neglect the latter. Then, for the liquid gallium under the present conditions we obtain from Eq. (1)

$$\mathbf{q} \approx -\rho c_p \kappa \nabla T. \tag{4}$$

Eq. (4) will be referred to below as assumption (i).

The thickness of the turbulent dynamic layer above the central part of the dead end can be estimated [11] as

$$\delta \sim \frac{d}{(V_0 d/v)^{1/5}}. \tag{5}$$

Taking for the estimate $d = 0.5 \times 10^{-2}$ m, $V_0 = 3$ m/s and $v = 27 \times 10^{-8}$ m^2/s, we obtain for GaIn $\delta \sim d/8.895 = 0.0562 \times 10^{-2}$ m, a small value compared to $H = 0.4 \times 10^{-2}$ m. Therefore, we can assume that heat transfer processes are practically unaffected by the viscous effects near the wall and proceed in the central part of the dead end against a background of pure stagnation flow. Thus in the axisymmetric case the velocity profile is given by

$$u = \gamma \frac{x}{2}, \quad v = -\gamma y, \tag{6a, b}$$

whereas in the planar case

$$u = \gamma x, \quad v = -\gamma y, \tag{7a, b}$$

where in both cases

$$\gamma = \frac{V_0}{H}. \tag{8}$$

Eqs. (6)–(8) will be referred to below as assumption (ii). Note that the velocity fields (6) and (7) satisfy the continuity equations

$$\frac{1}{x}\frac{\partial xu}{\partial x} + \frac{\partial v}{\partial y} = 0 \tag{9}$$

and

$$\frac{\partial u}{\partial x} + \frac{\partial v}{\partial y} = 0, \tag{10}$$

respectively, in the axisymmetric and planar cases.

In the central part of the dead end the temperature field depends only slightly on x, as suggested by the numerical and experimental data. This observation allows us to neglect $\partial^2 T/\partial x^2$ and $(1/x)\partial(xT)/\partial x$ relative to $\partial^2 T/\partial y^2$ in the central part of the flow. This will be referred to below as assumption (iii).

4.3. Calculation of the heat transfer coefficient and the Nusselt number

Under assumptions (i)–(iii), the temperature field in the central part of the dead end satisfies the following equation

$$\frac{\gamma x}{2}\frac{\partial T}{\partial x} - \gamma y \frac{\partial T}{\partial y} = \kappa \frac{\partial^2 T}{\partial y^2} \tag{11}$$

in the axisymmetric case. In the boundary layer approximation the solution is subjected to the boundary conditions

$$y = 0 \quad T = T_w, \tag{12a}$$

$$y = \infty \quad T = T_0. \tag{12b}$$

Eq. (11) can be converted into the standard form

$$\frac{\partial^2 T}{\partial y^2} + P(x) y \frac{\partial T}{\partial y} = Q(x) \frac{\partial T}{\partial x}, \tag{13}$$

where

$$P(x) = \frac{\gamma}{\kappa}, \quad Q(x) = \frac{\gamma x}{2\kappa}. \tag{14a, b}$$

The solution of the problem (12) and (13) is then given by [14]

$$T = T_0 + (T_w - T_0)\left[1 - \operatorname{erf}\left(\frac{Z}{2}\right)\right], \tag{15}$$

where

$$W(x) = 2 \cdot \int_{\text{const}}^{x} \frac{P(\xi)}{Q(\xi)} \mathrm{d}\xi, \tag{16a}$$

$$Z = y\left[\int_0^x \frac{\mathrm{e}^{W(\xi) - W(x)}}{Q(\xi)} \mathrm{d}\xi\right]^{-1/2}. \tag{16b}$$

Substituting Eqs. (14) in (16), we obtain

$$W = 4\ell n\xi - 4\ell n(\text{const}), \tag{17a}$$

$$Z = \frac{y}{\sqrt{\kappa/(2\gamma)}}. \tag{17b}$$

Eqs. (15) and (17b) yield

$$\left.\frac{\partial T}{\partial y}\right|_{y=0} = -(T_w - T_0)\frac{1}{\sqrt{\pi\kappa/(2\gamma)}}, \tag{18a}$$

$$q|_{y=0} = k(T_w - T_0)\frac{1}{\sqrt{\pi\kappa/(2\gamma)}}, \tag{18b}$$

where $k = \rho c_p \kappa$ is the thermal conductivity. On the other hand,

$$q|_{y=0} = h(T_w - T_0), \tag{19}$$

where h is the heat transfer coefficient. Combining Eqs. (18b) and (19), we obtain

$$h = k\sqrt{\frac{2\gamma}{\pi\kappa}}, \tag{20a}$$

$$Nu = \frac{hd}{k} = d\sqrt{\frac{2\gamma}{\pi\kappa}}. \tag{20b}$$

Substituting Eq. (8), we find from Eqs. (20)

$$h = \sqrt{\frac{2}{\pi}}\mathrm{k}\sqrt{\frac{V_0}{H\kappa}} = 0.798\mathrm{k}\sqrt{\frac{V_0}{H\kappa}}, \tag{21a}$$

$$Nu = \sqrt{\frac{2}{\pi}}Re^{1/2}Pr^{1/2}\left(\frac{d}{H}\right)^{1/2} = 0.798Re^{1/2}Pr^{1/2}\left(\frac{d}{H}\right)^{1/2}, \tag{21b}$$

where the Reynolds number is

$$Re = \frac{V_0 d}{\nu}. \tag{22}$$

Given, for example, $d = 0.8\times10^{-2}$ m and $H = 0.4\times10^{-2}$ m, we obtain

$$Nu = 1.13Re^{1/2}Pr^{1/2}. \tag{23}$$

For GaIn, the thermal conductivity $k = 41.8$ W/(m K) (Table 3) and the thermal diffusivity $\kappa = 1.324\times10^{-5}$ m^2/s. Taking $V_0 = 2.35$ m/s and $H = 0.4\times10^{-2}$ m, we obtain from Eq. (21a) $h = 22.22\times10^4$ W/(m^2 K). For $V_0 = 3.25$ m/s, $h = 26.13\times10^4$ W/(m^2 K).

When the value of q_w is given, and the temperature T_w is to be found, we obtain from Eqs. (19) and (21a)

$$T_w = T_0 + \frac{q_w}{0.798\mathrm{k}[V_0/(H\kappa)]^{1/2}}. \tag{24}$$

Taking $T_0 = 313$ K and $V_0 = 2.35$ m/s with all the other parameters as before, we obtain from Eq. (24) for $q_w = 14$ MW/m^2 the value of $T_w = 376$ K $= 103$ °C. For $T_0 = 313$ K, $V_0 = 3.25$ m/s and $q_w = 19$ MW/m^2 Eq. (24) yields $T_w = 385.7$ K $= 112.5$ °C.

The temperature inside the target at a distance ℓ from the dead-end bottom (the rear side of the target) is readily given by the solution of the thermal-conduction equation

$$T_\ell = T_w + \frac{q_w}{k_w}\ell, \tag{25}$$

where k_w is the thermal conductivity of the target material (molybdenum, $k_w = 126$ W/(m K)). Taking $\ell = 1$ mm, and using the values of T_w obtained above, we find for $q_w = 14$ MW/m^2 (and $V_0 = 2.35$ m/s) $T_\ell = 487.1$ K $=$ 214 °C. In the second case, with $q_w = 19$ MW/m^2 (and $V_0 = 3.25$ m/s) we find $T_\ell = 536.49$ K $= 263.34$ °C. The measurements in the midplane of the target in these two cases yield at $\ell = 1$ mm $T_{\ell1} \approx 230$ °C and 248 °C, respectively (cf. Section 3), which are in good agreement with the predictions.

Lienhard ([3] and references therein) solved numerically the potential problem on flow in an axisymmetric impinging jet with a free surface. Then, he matched the potential flow to the self-similar solution for a radially-spreading laminar boundary layer on the wall and calculated the corresponding heat transfer at the stagnation point. He approximated his numerical results for the laminar stagnation flow at low Prandtl numbers as $Nu = (2/\pi)^{1/2}\cdot(1.831)^{1/2}Re^{1/2}Pr^{1/2} = 1.08Re^{1/2}Pr^{1/2}$. This approximation is in remarkable agreement with the analytical results of the present work, given by Eqs. (21b) and (23).

In the planar case the governing equation becomes

$$\gamma x\frac{\partial T}{\partial x} - \gamma y\frac{\partial T}{\partial y} = \kappa\frac{\partial^2 T}{\partial y^2} \tag{26}$$

(cf. Eq. (7)), which can be recast into a standard form (13) with

$$P(x) = \frac{\gamma}{\kappa}, \quad Q(x) = \gamma\frac{x}{\kappa}. \tag{27}$$

In the present case we find from Eqs. (16a)

$$W = 2\ell n\xi - 2\ell n(\mathrm{const}). \tag{28}$$

However, using Eqs. (16b) and (28) we still obtain Z as per Eq. (17b). Then the temperature field is still given by Eqs. (15) and (17b), thus Eqs. (18)–(23) also hold in the planar case.

It is emphasized that the present theory predicts the heat transfer coefficient h and the Nusselt number Nu as independent of x, i.e. constant over the bottom of the dead end.

5. Numerical simulation of flow and heat transfer of liquid metals in a dead end

Numerical simulations were done for the GaIn alloy using the commercial code STAR-CD, in the case of axisymmetric flow and temperature distribution. The values of the physical parameters are listed in Table 3; the additional parameter is the specific heat of 326 J/(kg K).

In the numerical simulations the heat flux q_w at the bottom was assumed to be constant and given. It was applied at the front side of the disk-shaped target (2 mm thick, as in Section 3), where the temperatures were the highest. The heat transfer through the disk thickness was calculated, as well as the flow and heat transfer in the coolant impinging at the rear side of the disk (the dead end bottom). This yielded the temperature distribution throughout the whole disk, in particular in the mid-plane and at the rear side, where the temperatures were the lowest. The disk material was again molybdenum with thermal conductivity 126 W/(m K).

First, the flow and heat transfer were simulated as being fully laminar. In Fig. 6 the temperature distributions in the radial direction inside the target at depths (from the cooled rear side of the target) of $\ell = 0.88$ mm and 1.11 mm are shown for two cases of $V_0 = 2.35$ m/s, $q_w = 14$ MW/m^2 (Fig. 6a) and $V_0 = 3.25$ m/s, $q_w = 19$ MW/m^2 (Fig. 6b). These results show that laminar cooling with liquid GaIn alloy according to Fig. 6a yields $T_{\ell1} \approx 215$ °C at $x =$ 1 mm and $T_{\ell2} \approx 120.19$ °C at $x = 6$ mm interpolated to the mid-plane $\ell = 1$ mm. Note that the experimental results for this case are $T_{\ell1} \approx 230$ °C and $T_{\ell2} \approx 80$ °C. Similarly, Fig. 6b yields $T_{\ell1} \approx 271.54$ °C at $x = 1$ mm and $T_{\ell2} \approx$

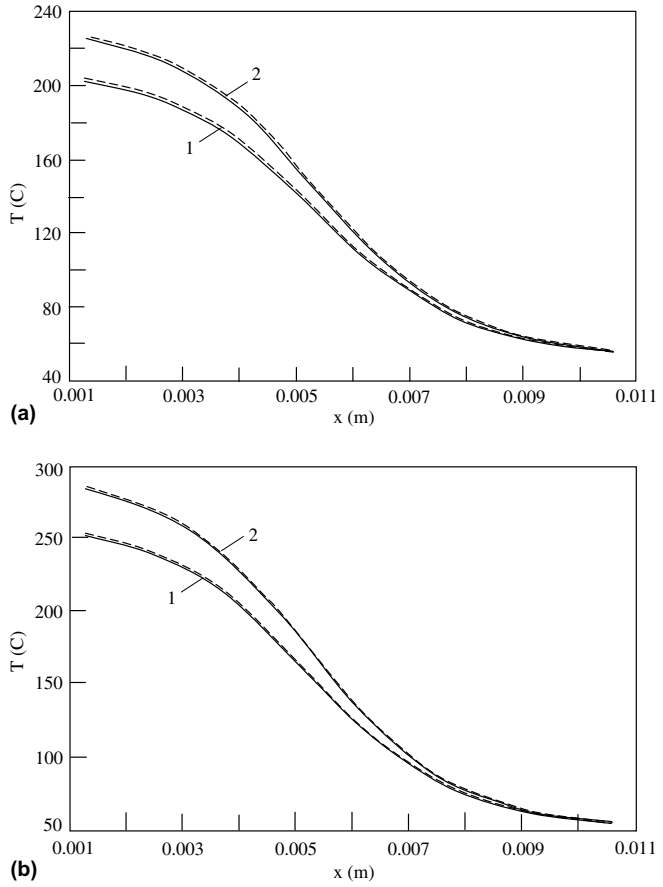

Fig. 6. The numerically simulated heat transfer (laminar flow) in the cases of: (a) $V_0 = 2.35$ m/s and $q_w = 14$ MW/m^2, and (b) $V_0 = 3.35$ m/s and $q_w = 19$ MW/m^2. Coolant is GaIn alloy. Curves 1 show the temperature distributions in the target at the depth of 0.88 mm from the cooled dead-end bottom (the rear side of the target), (2) at 1.11 mm. The results obtained with two different numerical algorithms are shown by solid and dashed lines which almost merge.

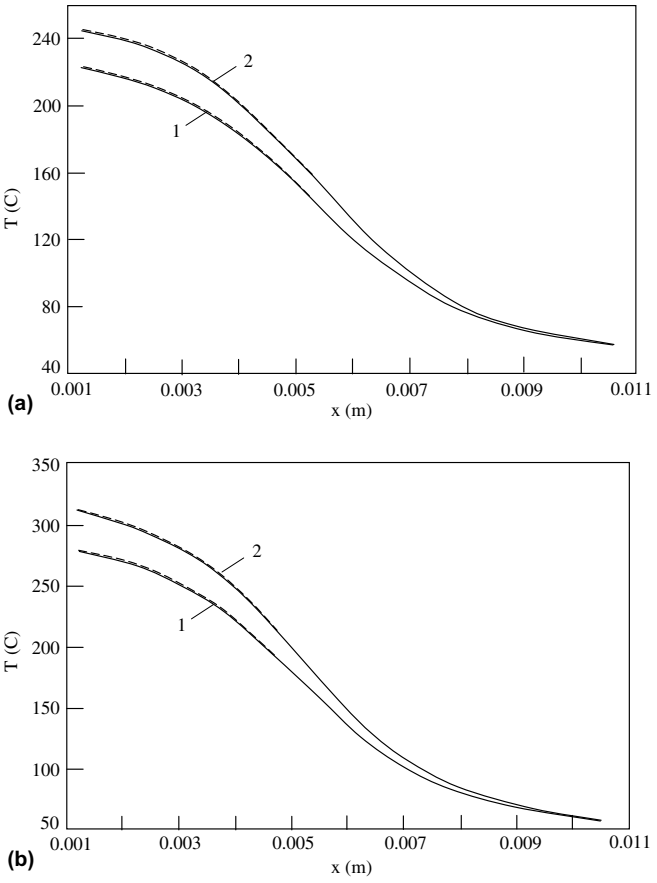

Fig. 7. The numerically simulated heat transfer (laminar flow) in the cases of: (a) $V_0 = 2.35$ m/s and $q_w = 14$ MW/m^2, and (b) $V_0 = 3.35$ m/s and $q_w = 19$ MW/m^2. Coolant is pure Ga. Curves 1 show the temperature distributions in the target at the depth of 0.88 mm from the cooled dead-end bottom (the rear side of the target), (2) at 1.11 mm. The results obtained with two different numerical algorithms are shown by solid and dashed lines which almost merge.

131.94 °C at $x = 6$ mm, while the measured values are $T_{\ell 1} \approx 248$ °C and $T_{\ell 2} \approx 85$ °C. Temperature at $x = 1$ mm, which is close to the stagnation point of the impinging jet, is higher than at the peripheral locations where convective heat removal is fully felt.

Thus the laminar version of STAR-CD is in reasonable agreement with the measured values at $x = 1$ mm, but significantly overestimates the temperature at $x = 6$ mm. The sensitivity of the predictions, to $a \pm 10\%$ variation of the measurement location ℓ, which can easily happen in these experiments, is about 20–30 °C (cf. Fig. 6a and b), which fails to explain the inaccurate predictions at $x = 6$ mm. The sensitivity to the numerical algorithm choice available in STAR-CD is negligibly small.

To estimate the possible effect of the alloy composition, we also calculated the laminar heat transfer, with the pure metal as coolant (the physical parameters of pure Ga are also given in Table 3). Comparing Figs. 6 and 7, we find a predicted increase of $T_{\ell 1}$ at $x = 1$ mm of about 20 °C in the case of Ga versus GaIn, which agrees with the lower thermal conductivity of the metal as compared with the alloy, while the value of $T_{\ell 2}$ at $x = 6$ mm is again significantly overpredicted.

For the numerical modeling of turbulence using STAR-CD, the k–ε model for high Reynolds numbers was chosen. It was tested against the other turbulence modeling options of STAR-CD, and the differences were not large. It was also checked whether the turbulence model covers the effects related to the molecular momentum and heat transfer, since the STAR-CD Manual does not specify that. For this purpose one of the molecular fluid parameters, say viscosity, was increased artificially in several simulations. The results were found to differ correspondingly, which proved that the turbulent options of the code account also for the molecular transfer effects.

The turbulent-flow calculations were done for GaIn. In Fig. 8 the velocity field over one half of the dead end is shown for the case of $V_0 = 2.35$ m/s, $q_w = 14$ MW/m^2. The corresponding result for the case of $V_0 = 3.25$ m/s, $q_w = 19$ MW/m^2 is shown in Fig. 9. The central part of the dead end (on the left in Figs. 8 and 9), where the outflowing jet impinges on the bottom, shows the characteristic

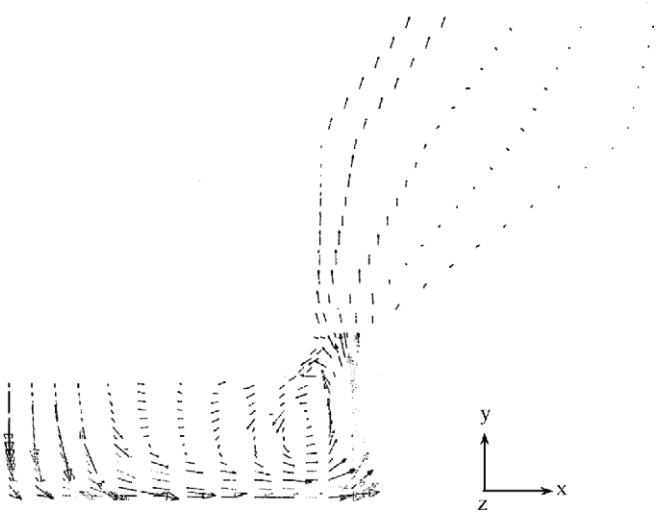

Fig. 8. The numerically simulated flow field in the case of $V_0 = 2.35$ m/s and $q_w = 14$ MW/m^2.

structure of the stagnation flow assumed in Section 4.2. Near the outer side of the dead end the flow turns back, so that the overall pattern can be characterized as closed-loop circulatory flow.

From the numerical calculations we obtained the temperature distribution at the bottom $T_w(x)$ and the corresponding local heat-flux transfer coefficient is found as per

$$h(x) = \frac{q_w}{T_w(x) - T_0}. \tag{29}$$

The calculated temperature distributions for the turbulent flow are shown in Figs. 10 and 11 corresponding to $V_0 = 2.35$ m/s, $q_w = 14$ MW/m^2 and to $V_0 = 3.25$ m/s, $q_w = 19$ MW/m^2, respectively. For the mid-plane (curve 2), Fig. 10 yields $T_{\ell 1} \approx 342$ °C at $x = 1$ mm and $T_{\ell 2} \approx 136$ °C at $x = 6$ mm. Note that for $V_0 = 2.25$ m/s and $q_w = 14$ MW/m^2 the experimental results are $T_{\ell 1} \approx 230$ °C and $T_{\ell 2} \approx 80$ °C (cf. Section 3). Similarly, Fig. 11 yields $T_{\ell 1} \approx 434$ °C at $x = 1$ mm and $T_{\ell 2} \approx 160$ °C at $x = 6$ mm.

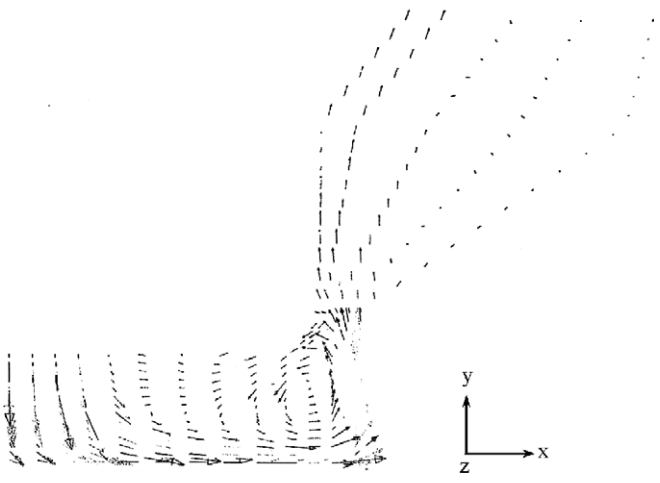

Fig. 9. The numerically simulated flow field in the case of $V_0 = 3.35$ m/s and $q_w = 19$ MW/m^2.

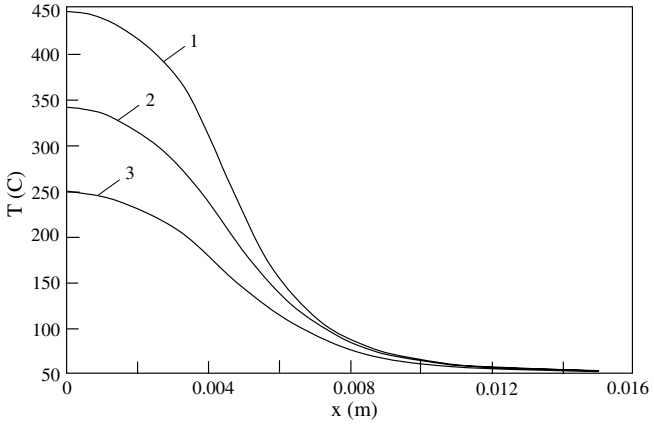

Fig. 10. The temperature distribution over: (1) the lower side of the disk (where the radiative heat flux q_w is imposed), (2) the mid-thickness of the disk, (3) the upper side of the disk (where the coolant jet impinges). $V_0 = 2.35$ m/s and $q_w = 14$ MW/m^2.

For $V_0 = 3.25$ m/s and $q_w = 19$ MW/m^2 the measured values are $T_{\ell 1} \approx 248$ °C and $T_{\ell 2} \approx 85$ °C.

The numerically calculated distributions of the heat transfer coefficient for the turbulent flows predicted using Eq. (29) and $T_w(x)$ for the rear side of the disk are shown in Fig. 12 together with the numerical predictions for the corresponding laminar cases. It is emphasized that STAR-CD predicts higher values of the heat transfer coefficient for laminar flows as compared to the corresponding turbulent flows.

The numerical results for the turbulent flow grossly overestimate the mid-plane temperatures $T_{\ell 1}$ and $T_{\ell 2}$ as compared to the experimental values. Moreover, the former are much higher than those predicted with the laminar flow model (cf. Figs. 6 and 7 versus Figs. 10 and 11, respectively). This is a clear indication that the turbulent model in STAR-CD grossly overestimates the turbulent viscosity in the case of liquid metal flow – as a result of which the flow velocity is reduced due to higher viscous dissipation, the

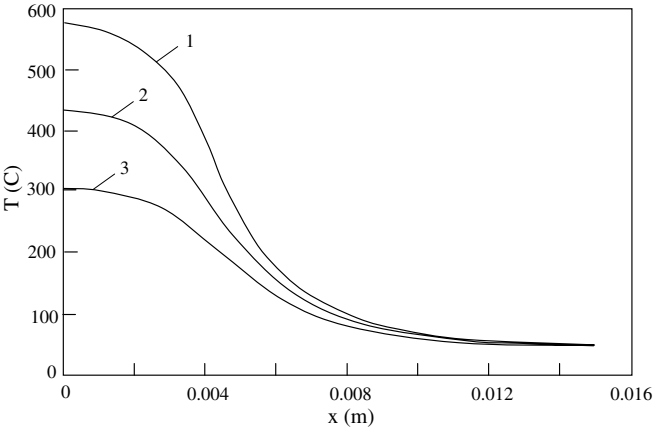

Fig. 11. The temperature distribution over: (1) the lower side of the disk (where the radiative heat flux q_w is imposed), (2) the mid-thickness of the disk, (3) the upper side of the disk (where the coolant jet impinges). $V_0 = 3.25$ m/s and $q_w = 19$ MW/m^2.

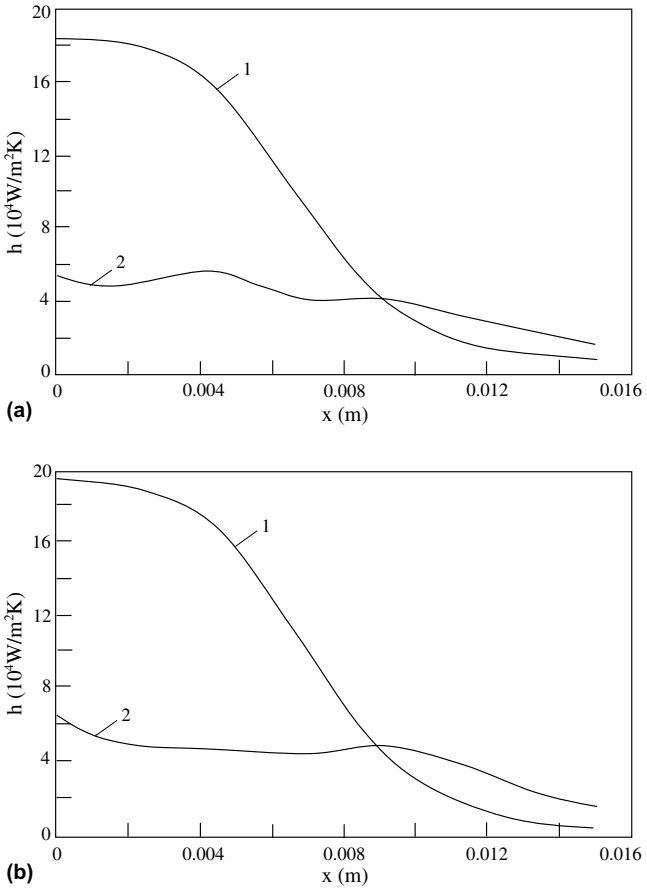

Fig. 12. The heat transfer coefficient at the rear side of the disk. (a) $V_0 = 2.35$ m/s and $q_w = 14$ MW/m^2, (b) $V_0 = 3.25$ m/s and $q_w = 19$ MW/m^2. Curves 1 correspond to the laminar flows, (2) to the turbulent ones.

heat transfer is reduced correspondingly (cf. Fig. 12), and the temperatures increase dramatically. A similar shortcoming of STAR-CD is indicated by the numerical results of Ref. [10]. Their calculations of cooling, in a geometry similar to that of the present work, resulted in marked underprediction of the heat transfer coefficient h in the case of liquid Ga compared to the experimental data (cf. Fig. 1 in Ref. [10]). On the other hand, the numerical results of Ref. [10] for a water-cooling system also based on STAR-CD, agree with the experimental data and can be considered as reliable.

6. Conclusion

A jet impingement liquid-metal cooling system for high heat-flux cooling was constructed and operated. The experiments demonstrate that the GaIn-based system is capable of dealing with heat fluxes of about 20 MW/m^2 over an area of 10^{-4} m^2 with a very low jet velocity – less than 4 m/s. A novel analytical theory, capable of predicting the cooling rates, is proposed, and direct numerical simulations were conducted. Agreement between the experimental data and the analytical model is fairly good.

The numerical results obtained using the commercial code STAR-CD for the case of laminar flow of the GaIn alloy, are also in reasonable agreement with the experimental data near the target center, but overestimate the measured temperatures at peripheral locations. For the case of turbulent flow, this code grossly underpredicts the heat removal rate and overpredicts the measured temperatures. The turbulence model of the code also grossly overpredicts the eddy viscosity for liquid metals, which in turn results in underprediction of the heat transfer rate. The conclusion is that STAR-CD is inapplicable in cases involving turbulent heat transfer in liquid metals.

References

[1] X. Liu, J.H. Lienhard, Extremely high heat flux removal by subcooled liquid jet impingement, Fundamentals of Subcooled Flow Boiling, 217, ASME, HTD, 1992, pp. 11–20.
[2] B.W. Blackburn, J.C. Yanch, R.E. Klinkowstein, Development of high-power water cooled Beryllium target for use in accelerator-based Boron neutron capture therapy, Med. Phys. 25 (1998) 1967–1974.
[3] J.H. Lienhard, Liquid Jet Impingement, Chapter, in: C.L. Tien (Ed.), Annual Review of Heat Transfer, 6, Begell House, New York, 1995.
[4] Y. Mitsutake, M. Monde, Ultra high critical heat-flux during forced flow boiling heat transfer with an impinging jet, Trans. ASME 125 (2003) 1038–1044.
[5] L. Zhen-Hua, T. Tie-Feng, Q. Yu-Hao, Critical heat flux of steady boiling for subcooled water jet impingement on the flat stagnation zone, Heat Transfer 126 (2004) 179–183.
[6] K. Sato, A. Furutani, M. Saito, M. Isozaki, K. Suganuma, S. Imahori, Melting attack of solid plates by a high-temperature liquid jet [II] – Erosion behavior by a molten metal jet, Nucl. Eng. Des. 132 (1991) 171–186.
[7] B.W. Blackburn, J.C. Yanch, Liquid Gallium cooling for a high-power Beryllium target for use in accelerator Boron neutron capture therapy (ABNCT), in: Proc. Eighth Workshop on Targetry and Target Chemistry, St. Louis, Missouri, 1999.
[8] B.W. Blackburn, High-power target development for accelerator based neutron capture theory, Ph.D. Thesis, MIT, Boston, MA, 2002.
[9] A. Miner, U. Ghoshal, Cooling of high-power-density microdevices using liquid metal coolants, Appl. Phys. Lett. 85 (2004) 506–508.
[10] I. Silverman, A. Nagler, High heat flux cooling with water jet impingement, 2004 ASME Heat Transfer/Fluids Engineering Summer Conference, Charlotte, NC, July 11–15, 2004.
[11] H. Schlichting, Boundary-Layer Theory, McGraw-Hill, New York, 1979.
[12] H. Gortler, Berchnung von Aufgaben der freier Turbulenz auf Grund eines nenen Naherungsansatzes, ZAMM 22 (1942) 244–254.
[13] L.A. Vulis, V.P. Kashkarov, Theory of Jets of Viscous Liquid, Nauka, Moscow, 1965 (in Russian).
[14] A.L. Yarin, G. Brenn, O. Kastner, D. Rensink, C. Tropea, Evaporation of acoustically levitated droplets, J. Fluid Mech. 399 (1999) 151–204.